Supporting information

Strategy to isomerization of dibenzo[b,d]furan based carbazole derivatives as hole transporting materials for perovskite solar cells: theoretical design and experimental study

Xin Chen[a], Jiayi Qi[a], Xin Jiang[a], Fei Wu[b,*], Xiaorui Liu[a,*]

[a]School of Chemistry and Chemical Engineering, Southwest University, Chongqing 400715, P.R. China

[b]Chongqing Key Laboratory for Advanced Materials and Technologies of Clean Energy, School of Materials and Energy, Southwest University, Chongqing 400715, P. R. China

*Corresponding authors: E-mail: feiwu610@swu.edu.cn (F. Wu); liuxiaorui@swu.edu.cn (X. Liu)

S1. Experimental Section

S1.1 Computational Details

The ground state structures of the studied molecules CX11-CX14 were optimized using the B3P86/6-311G(d,p) functional and basis set[1,2]. The optimized structures did not exhibit any imaginary frequencies. Based on these optimized structures, the HOMO and LUMO energy levels of CX11-CX14 were calculated.

The electron affinity and absolute hardness were calculated using the B3P86/6-311G(d,p) level. Additionally, UV-visible absorption spectra of CX11-CX14 in dichloromethane solution were computed using the TD-PBE0/6-31G(d) functional and basis set[3].

Reorganization energy, a key parameter for calculating electron transfer rates based on Marcus theory, is divided into internal reorganization energy, which measures changes in the system after altering electronic states, and external reorganization energy, which is influenced by external factors. For the studied molecules, the internal reorganization energy of holes is significantly larger than the external reorganization energy. The λ_h parameter was obtained using the adiabatic potential energy surface method at the B3P86/6-311G(d,p) level. DFT and TD-DFT calculations were performed using Gaussian 09 software[4].

A 7×7×3 $FAPbI_3$ perovskite unit cell was constructed, with a vacuum layer height of 95 Å. The surface model box was sized at 44.5 × 44.5 × 90.0 Å, and 36 HTM molecules were randomly placed on the initial perovskite model using Packmol[5,6]. Under the NVT ensemble, molecular dynamics (MD) simulations were conducted to observe the distribution and arrangement of HTMs on the perovskite surface through the Gromacs program[7]. To simulate realistic device fabrication conditions, the system was annealed from an initial temperature of 0 K, heated to 400 K over 100 ps, held at 400 K for 500 ps, and then cooled to 300 K over 100 ps until the end of the simulation. The cutoff distance for van der Waals interactions was set to 1.2 nm. The total simulation run time was 10 ns, and the results were visualized using VMD. The simulation was assisted by Multiwfn, VASP, and Sobtop programs[6,8–13]. Additionally, detailed information on the calculations of charge transfer integral (v), charge transfer rate (K), and hole mobility (μ_h) from previous work was simulated using the ADF program with the PW91/TZP functional and basis set[14].

In the Vienna Ab Initio Simulation Package (VASP), the interface systems of perovskite and HTMs (CX11-CX14) were optimized using the Generalized Gradient Approximation (GGA) and

the Perdew-Burke-Ernzerhof (PBE) exchange-correlation functional. The plane wave cutoff energy was set to 400 eV. For k-point sampling, a 1×1×1 Monkhorst-Pack grid was applied to the irreducible Brillouin zone. The convergence threshold for self-consistent iterations was set to 1.0×10^-4 eV/atom, with atomic positions fully relaxed until the maximum force on each atom was less than 0.05 eV/Å. Non-self-consistent calculations were then performed, and charge density files were processed to obtain charge difference density maps (CDD), adsorption energies and electron localization function (ELF)[15–17].

Energy Decomposition Analysis (EDA) was performed using the Gaussian program and Multiwfn program under the B3LYP-D3(BJ)/6-31+G(d,p) conditions[18]. The IRI maps were generated by combining the Multiwfn wave function analysis program with the VMD visualization program, visualizing the interactions between CX11-CX14 molecules[19].

S1.2 Device Fabrication

To measure the photovoltaic performance of PSCs, a structure of FTO/TiO_2/SnO_2/$FAPbI_3$/HTMs/Ag was fabricated. The etched FTO glass substrates were first ultrasonically cleaned in detergent, deionized water, and anhydrous ethanol for 30 minutes each, then dried with a flow of air. The FTO substrates were heated to 450°C, and a dense TiO_2 solution (2 M acetylacetone and 0.2 M isopropanol titanium isopropoxide solution) was sprayed 3-4 times, then SnO_2 solution spin-coated at 4000 rpm for 30 seconds.[20]

The FTO substrates were then transferred to an N_2 glove box. The PbI_2 precursor solution with 1.5 M concentration was prepared by adding PbI_2 into a mixed DMF/DMSO (V:V=9:1) solvent and stirring at 70 °C for overnight. Meanwhile, organic ammonium salt solution contained FAI, MABr and MACl (weight ratio of 90mg:9mg:9mg) in 1 mL IPA solvent were prepared. During the first-step, 30 μL PbI_2 solution was poured on the TiO_2/SnO_2 substrate and spinning with 1500 rpm for 30 s, then quickly annealing at 70 °C for 1 min and bright yellow films were obtained. Subsequently, organic ammonium salt solution spinning-coated on PbI_2 film at 1800 rpm for 30 s, the prepared films were quickly transferred and annealing at 150 °C for 15 min in air atmosphere with RH=~40%. CHEAI solution (3 mg/mL) was spin-coated on the perovskite film at 6000 rpm for 30 s, and then the film was annealed at 100 °C for 5 min. The Spiro-OMeTAD solution containing 72.3 mg Spiro-MeOTAD, 28.8 μL tBP, and 17.5 μL Li-TFSI (520 mg mL-1 in ACN), and CX11-CX14 was dissolved in chlorobenzene at a concentration of 60 mg/mL, Among them, 35.85 μL t-BP and 21.78

μL Li-TFSI (520 mg mL^{-1} in ACN) were added per 1mL HTMs solution. The HTMs solution spin-coated on the top of CHEAI layer at 4000 rpm for 30 seconds. After coating, the substrates were placed in a vacuum environment (<10^{-5} Pa) and a 100 nm thick silver electrode was deposited by thermal evaporation.

S1.3 The space-charge-limited current (SCLC) hole mobility measurements.

Pure hole devices were fabricated using the ITO/PEDOT:PSS/HTM/Ag structure. The dark J-V characteristics of the devices were measured in a nitrogen atmosphere within a glovebox. PEDOT:PSS was spin-coated onto the ITO substrates at 5000 rpm for 30 seconds and then annealed at 120°C for 30 minutes. The spin-coating conditions for the HTMs were consistent with those used for device fabrication. The mobility data were extracted from the current density-voltage (J-V) curves using the space-charge-limited current (SCLC) fitting method.

$$J = 9\varepsilon_\theta \varepsilon_\gamma \mu_h V^2 / 8L^3$$

According to the above equation, where J is the current density, ε_θ is the permittivity of free space, ε_γ is the relative dielectric constant of the transport medium, , μ_h is the hole mobility, V is the internal voltage of the device, L is the film thickness. ($\varepsilon_\gamma = 3$ for organic materials, ε_γ=8.85×10^{-12} F m^{-1}).

S1.4 Measurements

The ^{1}H nuclear magnetic resonance (^{1}H NMR) and the ^{13}C nuclear magnetic resonance (^{13}C NMR) spectra were obtained from a BRUKER AVANCE NEO 400 MHz NMR Instrument (in DMSO-d_6, 99.8%, Beijing Hwrkchemical Co., Ltd.). Mass spectra were collected on LCMS-IT-TOF mass spectrometer. UV-vis absorption spectra were measured on a Shimadzu UV-2450 absorption spectrophotometer. Absorption spectra in solution were recorded in dichloromethane solution with an HTM concentration of 10^{-5} M. Cyclic voltammetry studies were conducted using a CHI660E system in a typical three-electrode cell with a glass carbon working electrode, a platinum wire counter electrode, and a silver/silver chloride (Ag/AgCl) reference electrode. All electrochemical experiments were carried out under a nitrogen atmosphere at room temperature in an electrolyte solution of 0.1 M tetrabutylammonium hexa-fluorophosphate (Bu_4NPF_6) in dichloromethane at a sweeping rate of 50 mV s^{-1}. The potential of Ag/AgCl reference electrode was internally calibrated by using the ferrocene/ferrocenium redox couple (Fc/Fc^+). According to the onset oxidation potential of the CV measurements, the highest occupied molecular orbital (HOMO)

was estimated based on the vacuum energy level of ferrocene (5.1 eV): HOMO = – (E_{onset} – $E_{Fc/Fc+}$) – 5.1 eV. The current–voltage (*J–V*) curves were measured under 100 mW cm^{-2} (AM 1.5 G) simulated sunlight using Keithley 2400 in conjunction with a Newport solar simulator (94043A). Film thickness of hole transport layer and perovskite layer were measured by Surfcorder ET200A, Kosaka Laboratory Ltd. Using atomic force microscopy (AFM) to characterize the morphology, the model is CSPM5500A. Steady-state PL spectra were recorded on Fluorolog®-3 fluorescence spectrometer (Horiba). Time-resolved PL decay curves were measured by a single photon counting spectrometer from Horiba Instruments (Fluorolog®-3) with a Picosecond Pulsed UV-LASTER (LASTER375) as the excitation source. The top view of the sample was monitored by a field emission scanning electron microscope (FESEM. Sigma500).

S1.5 Synthesis of HTMs

CX11-CX14 was synthesized in a one-step reaction using the Suzuki-Miyaura coupling method, with the synthesis route shown in **Figure S4**.

9-(4-(dibenzo[b,d]furan-4-yl)phenyl)-N3,N3,N6,N6-tetrakis(4-methoxyphenyl)-9H-carbazole-3,6-diamine (CX11)： After assembling the apparatus, vacuum was applied and replaced with argon three times. Under argon protection, 9-(4-bromophenyl)-N^3,N^3,N^6,N^6-tetrakis(4-methoxyphenyl)-9H-carbazole-3,6-diamine (0.2330 g, 0.3 mmol), dibenzo[b,d]furan-4-yl(hydroperoxy)(hydroxy)borane (0.1030 g, 0.45 mmol), and the catalyst $Pd(PPh_3)_4$ (0.0347 g, 0.03 mmol) were added to a 100 mL three-neck flask. Then, 15 mL of pre-deoxygenated dioxane and 2 mL of potassium carbonate aqueous solution (2 M) were added. The reaction was stirred and refluxed at 100°C for 12 hours, then cooled to room temperature. The crude product was extracted with dichloromethane, and the organic layer was dried over anhydrous sodium sulfate. The solvent was removed using a rotary evaporator, and the crude product was purified by silica gel column chromatography using a petroleum ether:ethyl acetate (10:1) eluent to obtain a yellow solid powder (0.2257 g, 87.14%). ^{1}H NMR (600 MHz, DMSO-d_6) δ 8.25 – 8.17 (m, 4H), 7.82 (d, *J* = 7.5 Hz, 1H), 7.77 (t, *J* = 7.5 Hz, 3H), 7.72 (s, 2H), 7.59 – 7.53 (m, 2H), 7.46 (t, *J* = 7.5 Hz, 1H), 7.40 (d, *J* = 8.8 Hz, 2H), 7.11 (dd, *J* = 8.8, 2.2 Hz, 2H), 6.87 (d, *J* = 8.9 Hz, 8H), 6.81 (d, *J* = 9.1 Hz, 8H), 3.69 (s, 12H). ^{13}C NMR (151 MHz, DMSO) δ 155.94, 154.81, 153.02, 142.39, 141.88, 137.54, 137.11, 135.09, 130.57, 128.33, 127.43, 127.35, 125.03, 124.97, 124.58, 124.46, 124.33, 124.00, 123.97, 123.80, 121.78, 121.18, 116.95, 115.16, 112.27, 111.33, 55.65, 40.01, 0.57. MS: m/z= 863.3346,

calcd for C58H45N3O5: 863.3359.

9-(4-(dibenzo[b,d]furan-3-yl)phenyl)-N3,N3,N6,N6-tetrakis(4-methoxyphenyl)-9H-carbazole-3,6-diamine (CX12): After assembling the apparatus, vacuum was applied and replaced with argon three times. Under argon protection, 9-(4-bromophenyl)-N^3,N^3,N^6,N^6-tetrakis(4-methoxyphenyl)-9H-carbazole-3,6-diamine (0.2330 g, 0.3 mmol), dibenzo[b,d]furan-3-yl(hydroperoxy)(hydroxy)borane (0.1030 g, 0.45 mmol) , and the catalyst $Pd(PPh_3)_4$ (0.0347 g, 0.03 mmol) were added to a 100 mL three-neck flask. Then, 15 mL of pre-deoxygenated dioxane and 2 mL of potassium carbonate aqueous solution (2 M) were added. The reaction was stirred and refluxed at 100°C for 12 hours, then cooled to room temperature. The crude product was extracted with dichloromethane, and the organic layer was dried over anhydrous sodium sulfate. The solvent was removed using a rotary evaporator, and the crude product was purified by silica gel column chromatography using a petroleum ether:ethyl acetate (8:1) eluent to obtain a yellow solid powder (0.2160 g, 82.47%).^{1}H NMR (600 MHz, DMSO-d_6) δ 8.30 – 8.22 (m, 1H), 8.19 (d, J = 6.3 Hz, 1H), 8.15 – 8.01 (m, 3H), 7.84 (d, J = 2.8 Hz, 1H), 7.78 – 7.66 (m, 5H), 7.55 (t, J = 7.7 Hz, 1H), 7.46 – 7.41 (m, 1H), 7.38 (dd, J = 16.3, 6.6 Hz, 2H), 7.10 (d, J = 9.3 Hz, 2H), 6.92 – 6.76 (m, 16H), 3.70 (d, J = 10.7 Hz, 12H), 1.39 (s, 1H), 0.85 (s, 1H). ^{13}C NMR (151 MHz, DMSO) δ 156.73, 156.44, 154.80, 142.39, 141.85, 139.40, 139.20, 137.50, 136.96, 129.15, 128.21, 127.45, 124.98, 124.44, 123.99, 123.79, 123.76, 123.53, 122.58, 122.10, 121.77, 116.99, 115.16, 112.17, 111.29, 110.20, 55.64, 40.00. MS: m/z= 863.3344, calcd for C58H45N3O5: 863.3359.

9-(4-(dibenzo[b,d]furan-2-yl)phenyl)-N3,N3,N6,N6-tetrakis(4-methoxyphenyl)-9H-carbazole-3,6-diamine (CX13): After assembling the apparatus, vacuum was applied and replaced with argon three times. Under argon protection, 9-(4-bromophenyl)-N^3,N^3,N^6,N^6-tetrakis(4-methoxyphenyl)-9H-carbazole-3,6-diamine (0.2330 g, 0.3 mmol), dibenzo[b,d]furan-2-yl(hydroperoxy)(hydroxy)borane (0.1030 g, 0.45 mmol) , and the catalyst $Pd(PPh_3)_4$ (0.0347 g, 0.03 mmol) were added to a 100 mL three-neck flask. Then, 15 mL of pre-deoxygenated dioxane and 2 mL of potassium carbonate aqueous solution (2 M) were added. The reaction was stirred and refluxed at 100°C for 12 hours, then cooled to room temperature. The crude product was extracted with dichloromethane, and the organic layer was dried over anhydrous sodium sulfate. The solvent was removed using a rotary evaporator, and the crude product was purified by silica gel column chromatography using a petroleum ether:ethyl acetate (10:1) eluent to obtain a yellow solid powder

(0.2235 g, 90.71%).^{1}H NMR (600 MHz, DMSO-d_6) δ 8.05 (t, J = 6.2 Hz, 3H), 7.96 – 7.91 (m, 1H), 7.85 – 7.70 (m, 9H), 7.62 (d, J = 8.3 Hz, 1H), 7.57 (t, J = 8.0 Hz, 2H), 7.54 – 7.43 (m, 5H), 7.42 (d, J = 2.5 Hz, 1H), 7.38 (d, J = 8.9 Hz, 2H), 7.34 (t, J = 7.5 Hz, 1H), 7.14 – 7.10 (m, 2H), 6.89 (d, J = 8.5 Hz, 8H), 6.83 (d, J = 8.7 Hz, 8H), 3.70 (s, 12H). ^{13}C NMR (151 MHz, DMSO) δ 156.54, 156.46, 154.81, 153.96, 142.41, 129.44, 129.06, 127.77, 127.48, 127.01, 124.44, 124.36, 123.73, 123.05, 121.54, 116.16, 115.18, 112.37, 112.25, 112.02, 106.40, 55.66, 39.98. MS: m/z= 863.3344, calcd for C58H45N3O5: 863.3359.

9-(4-(dibenzo[b,d]furan-1-yl)phenyl)-N3,N3,N6,N6-tetrakis(4-methoxyphenyl)-9H-carbazole-3,6-diamine (CX14): After assembling the apparatus, vacuum was applied and replaced with argon three times. Under argon protection, 9-(4-bromophenyl)-N^3,N^3,N^6,N^6-tetrakis(4-methoxyphenyl)-9H-carbazole-3,6-diamine (0.2330 g, 0.3 mmol), dibenzo[b,d]furan-1-yl(hydroperoxy)(hydroxy)borane (0.1030 g, 0.45 mmol) , and the catalyst $Pd(PPh_3)_4$ (0.0347 g, 0.03 mmol) were added to a 100 mL three-neck flask. Then, 15 mL of pre-deoxygenated dioxane and 2 mL of potassium carbonate aqueous solution (2 M) were added. The reaction was stirred and refluxed at 100°C for 12 hours, then cooled to room temperature. The crude product was extracted with dichloromethane, and the organic layer was dried over anhydrous sodium sulfate. The solvent was removed using a rotary evaporator, and the crude product was purified by silica gel column chromatography using a petroleum ether:ethyl acetate (8:1) eluent to obtain a yellow solid powder (0.1952 g, 79.22%).^{1}H NMR (600 MHz, DMSO-d_6) δ 7.90 (d, J = 7.9 Hz, 2H), 7.85 – 7.72 (m, 6H), 7.67 – 7.62 (m, 2H), 7.52 (t, J = 7.8 Hz, 1H), 7.48 (d, J = 8.8 Hz, 2H), 7.43 (d, J = 7.5 Hz, 1H), 7.29 (t, J = 7.6 Hz, 1H), 7.16 – 7.12 (m, 2H), 6.90 (d, J = 8.5 Hz, 8H), 6.83 (d, J = 8.7 Hz, 8H), 3.70 (s, 12H). ^{13}C NMR (151 MHz, DMSO) δ 156.29, 156.14, 154.82, 142.39, 141.93, 138.40, 137.49, 137.32, 136.95, 130.92, 128.28, 128.17, 127.25, 125.00, 124.75, 124.47, 124.04, 123.48, 123.34, 122.40, 121.31, 116.94, 115.17, 112.32, 111.50, 111.38, 55.65, 40.01, 0.57. MS: m/z= 863.3345, calcd for C58H45N3O5: 863.3359.

S2. Figures

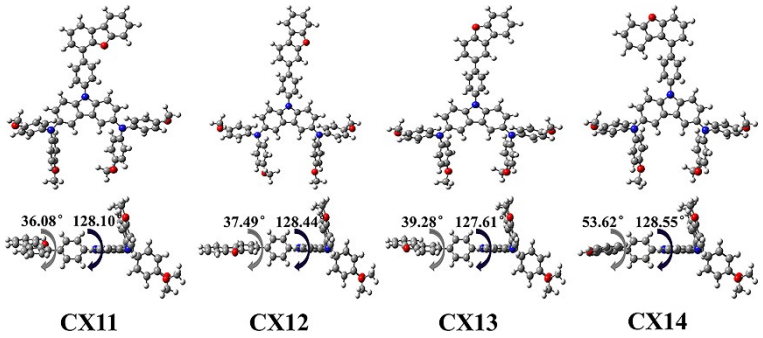

Figure S1. Optimized geometries of CX11-CX14 from the B3P86/6-311G(d,p) method and basis set.

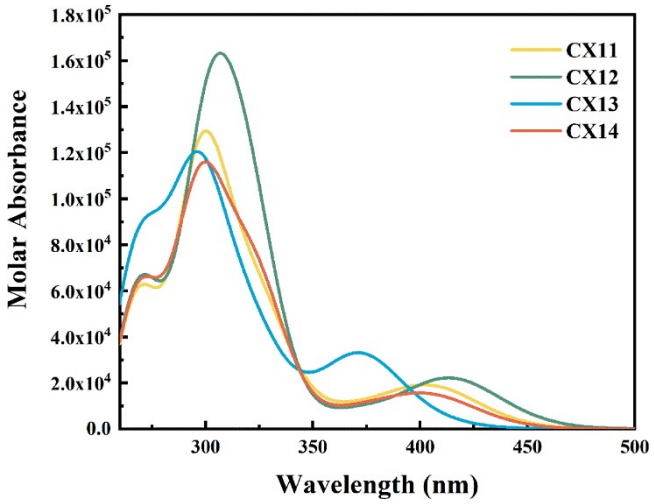

Figure S2 Simulated absorption spectra of molecules CX11-CX14 in dichloromethane (DCM).

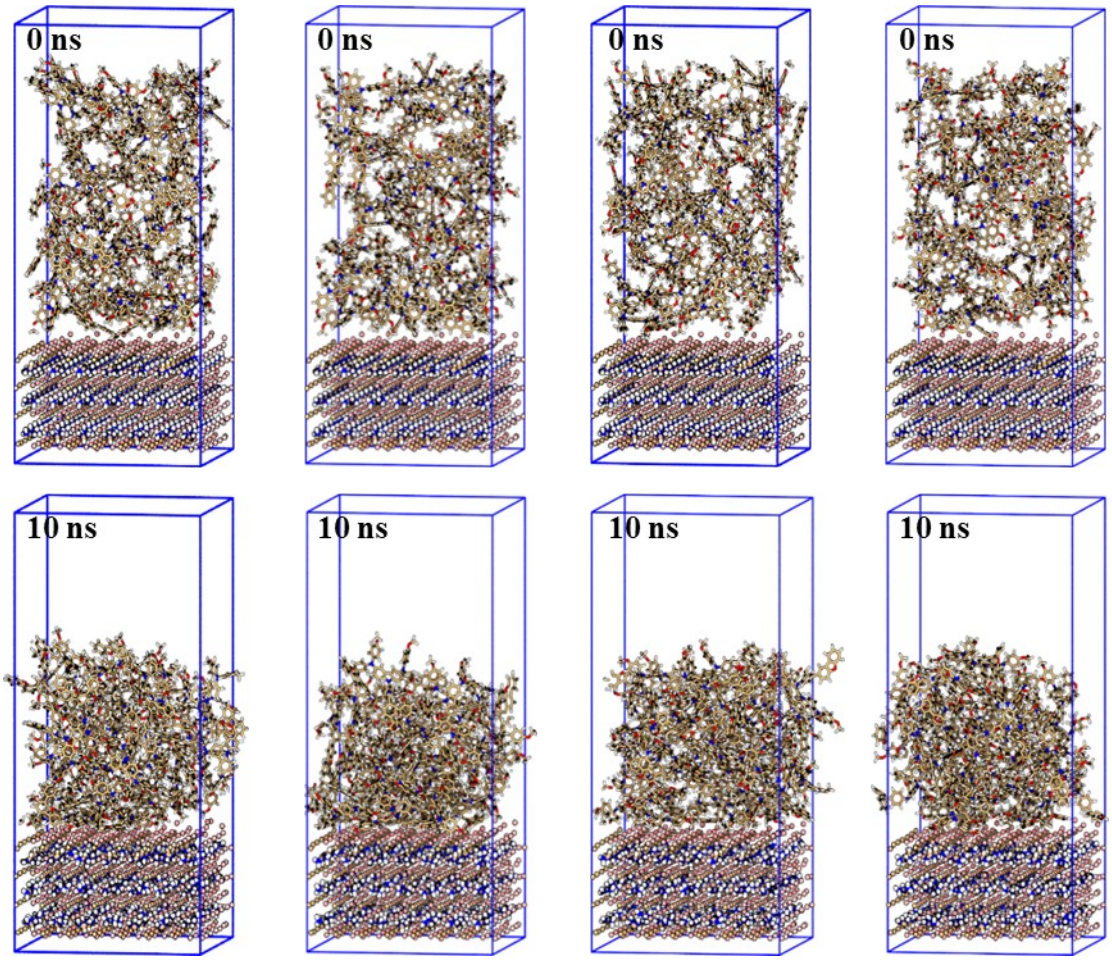

Figure S3 Distribution of CX11-CX14 on the perovskite surface after 10 ns of MD simulation.

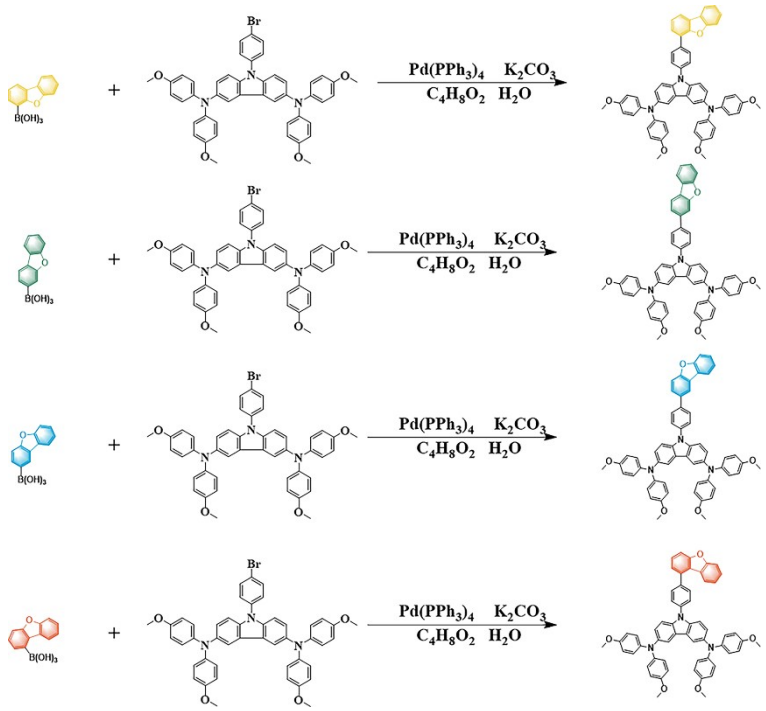

Figure S4. Synthesis route of CX11-CX14.

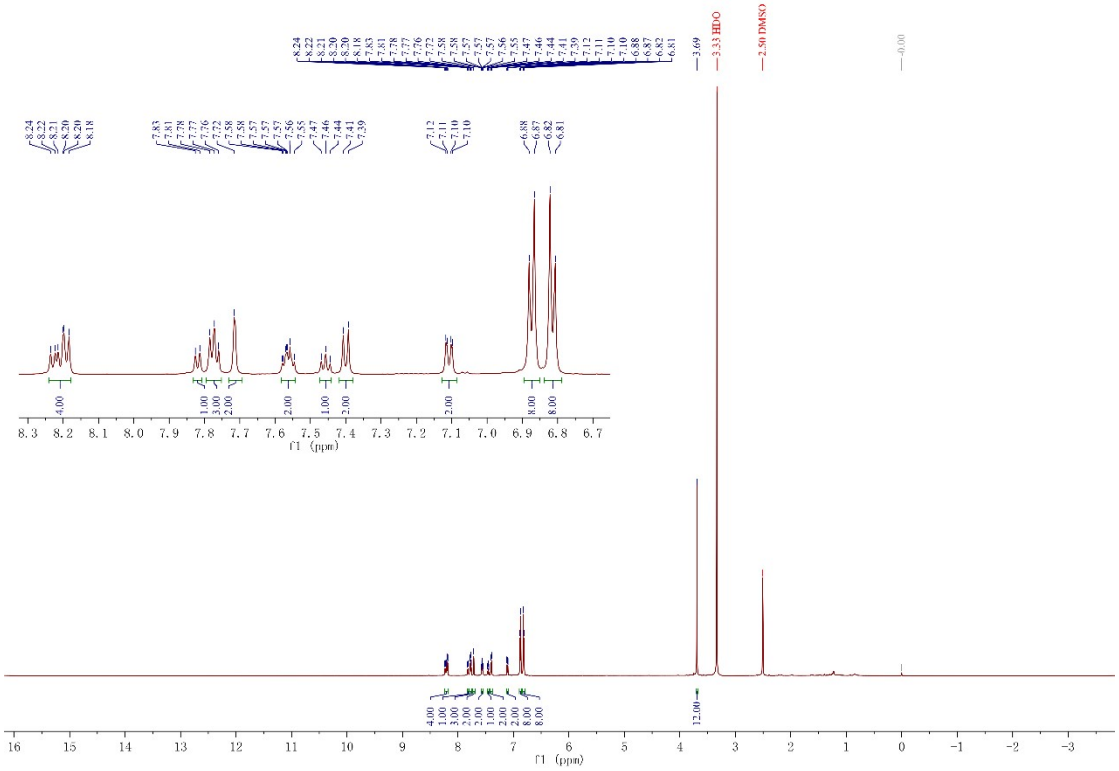

Figure S5. ^{1}H NMR spectrum of CX11 in DMSO.

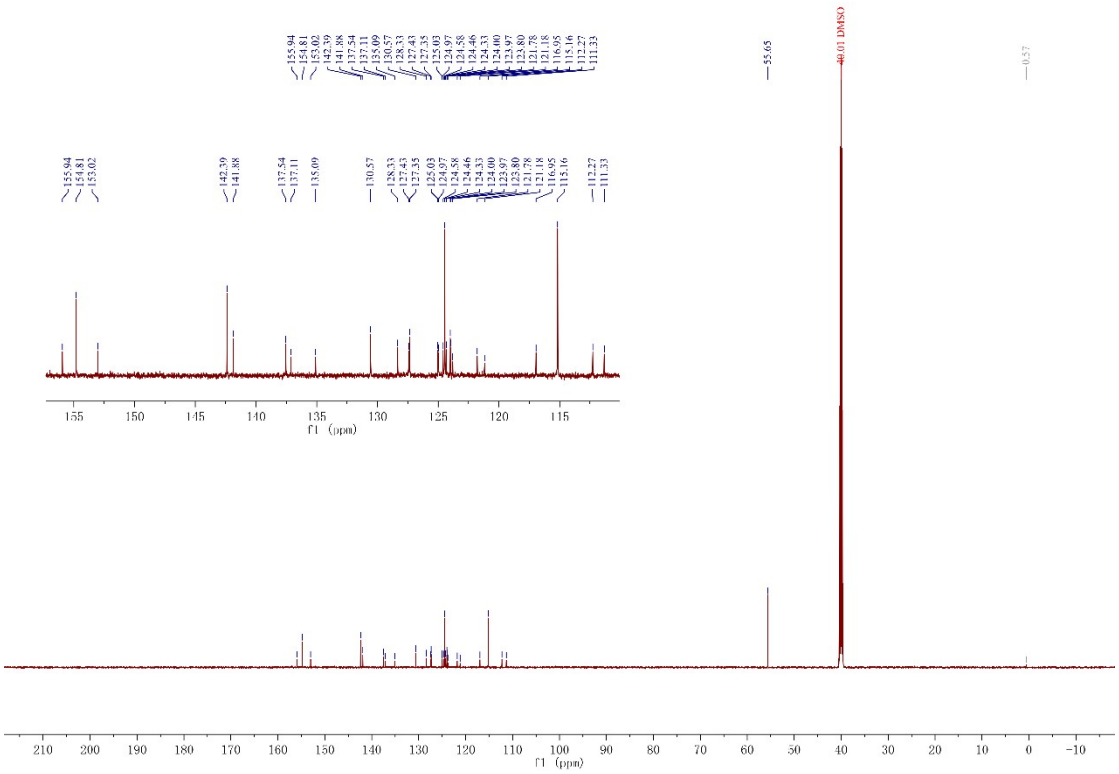

Figure S6. ^{13}C NMR spectrum of CX11 in DMSO.

Comment

Acquisition Paramet

Source Type	ESI	Ion Polarity	Positive	Set Nebulizer	0.4 Bar
Focus	Active	Set Capillary	4500 V	Set Dry Heater	180 °C
Scan Begin	50 m/z	Set End Plate	-500 V	Set Dry Gas	4.0 l/min
Scan End	1300 m/z	Set Charging	2000 V	Set Divert Valve	Source
		Set Corona	0 nA	Set APCI Heater	0 °C

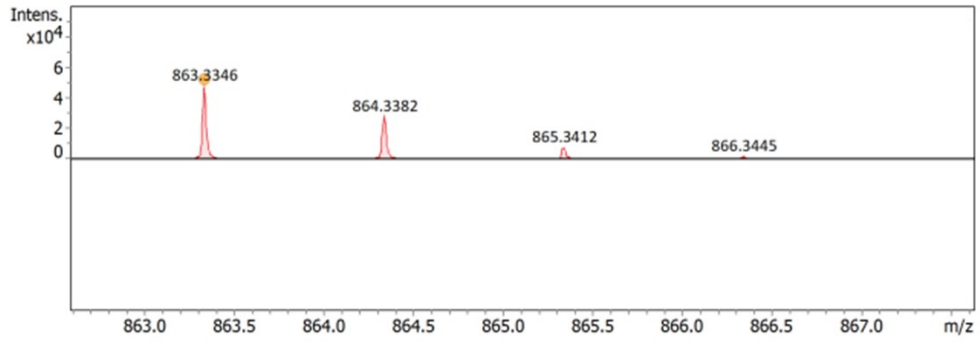

Meas. m/z	#	Ion Formula	m/z	err [ppm]	mSigma	# mSigma	Score	rdb	e¡¥ Conf	N-Rule
863.3346	1	C58H45N3O5	863.3359	1.6	41.8	1	100.00	38.0	even	ok

Figure S7. High resolution mass spectrometry of CX11.

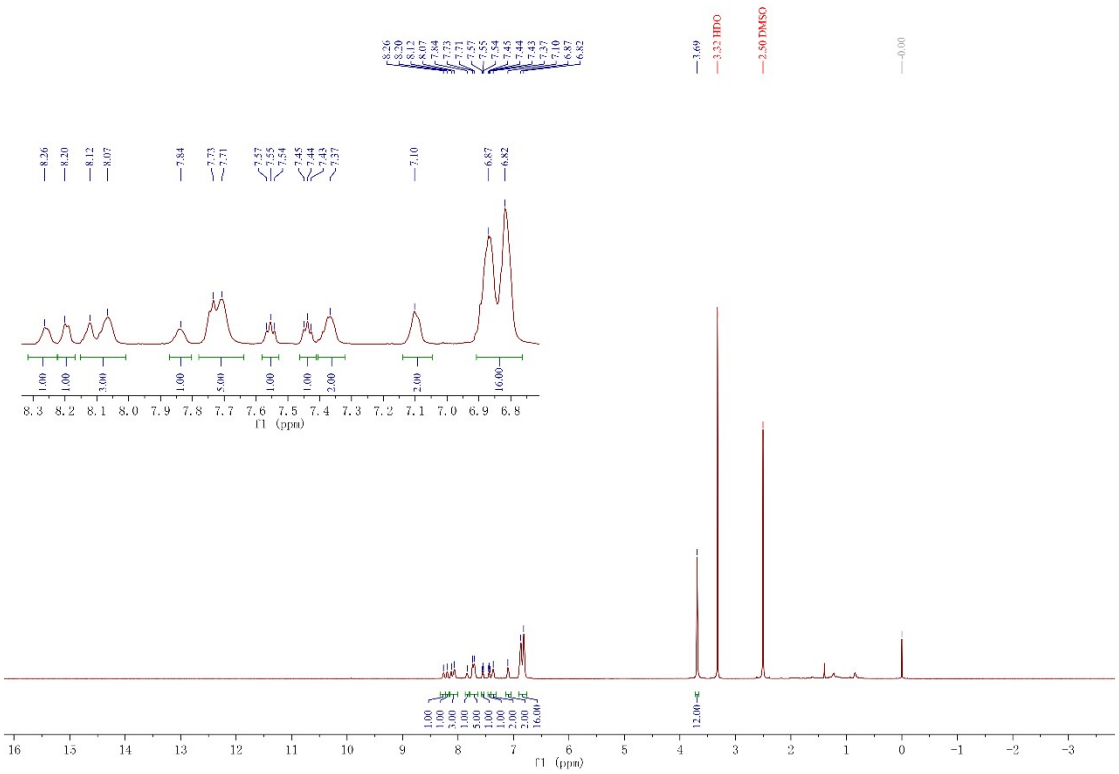

Figure S8. ^{1}H NMR spectrum of CX12 in DMSO.

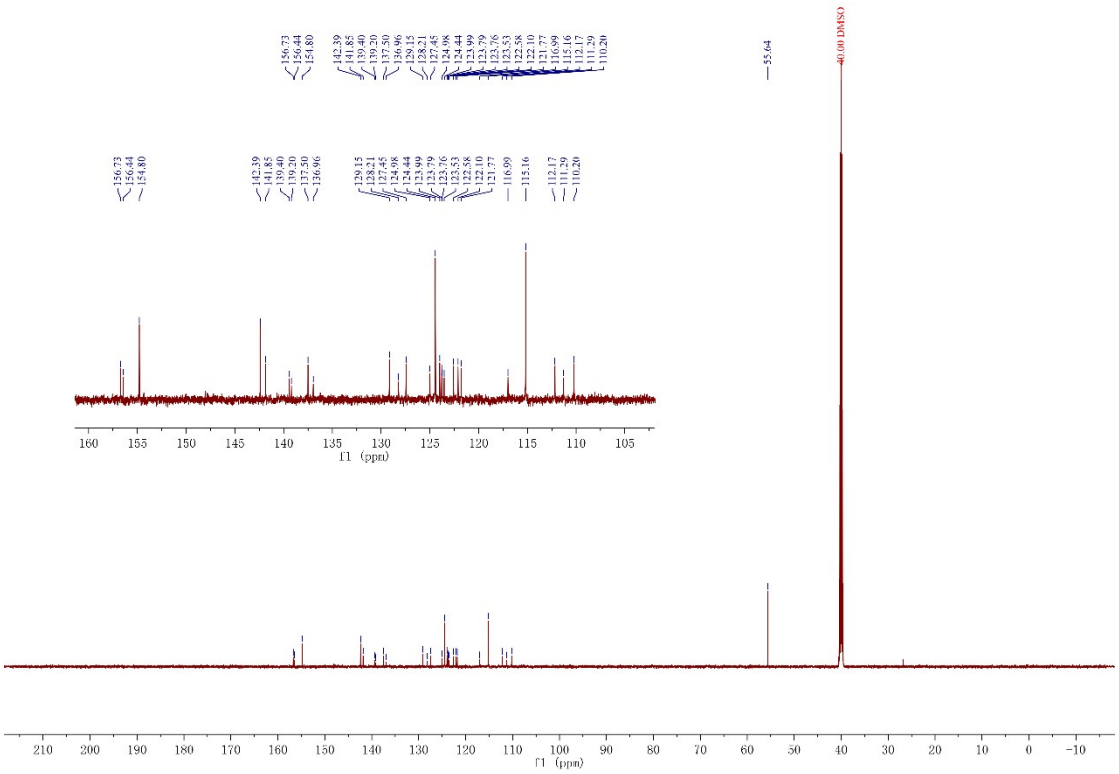

Figure S9. ^{13}C NMR spectrum of CX12 in DMSO.

Comment

Acquisition Paramet

Source Type	ESI	Ion Polarity	Positive	Set Nebulizer	0.4 Bar
Focus	Active	Set Capillary	4500 V	Set Dry Heater	180 °C
Scan Begin	50 m/z	Set End Plate	-500 V	Set Dry Gas	4.0 l/min
Scan End	1300 m/z	Set Charging	2000 V	Set Divert Valve	Source
		Set Corona	0 nA	Set APCI Heater	0 °C

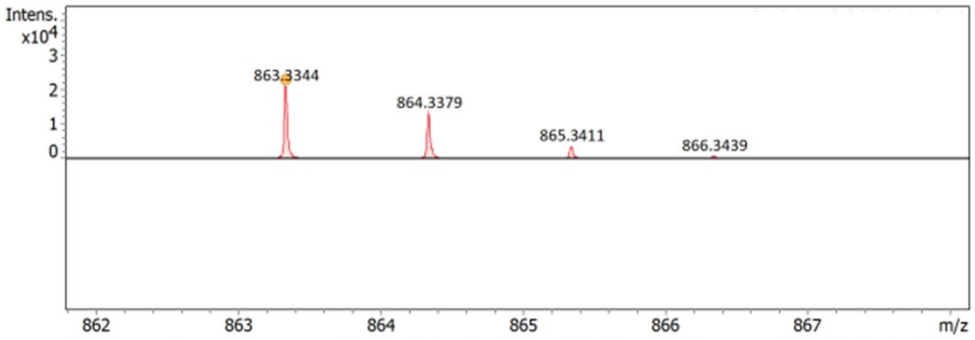

Meas. m/z	#	Ion Formula	m/z	err [ppm]	mSigma	#	mSigma	Score	rdb	e¡¥	Conf	N-Rule
863.3344	1	C58H45N3O5	863.3359	1.8	25.1		1	100.00	38.0	even		ok

Figure S10. High resolution mass spectrometry of CX12.

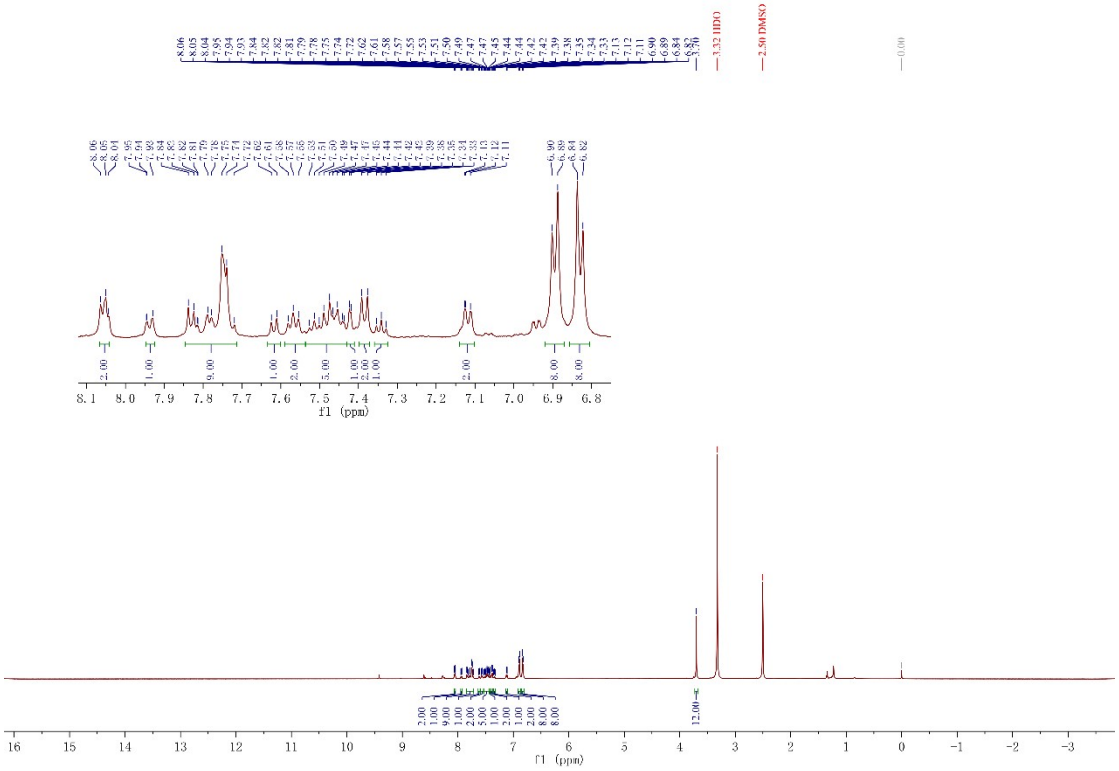

Figure S11. ^{1}H NMR spectrum of CX13 in DMSO.

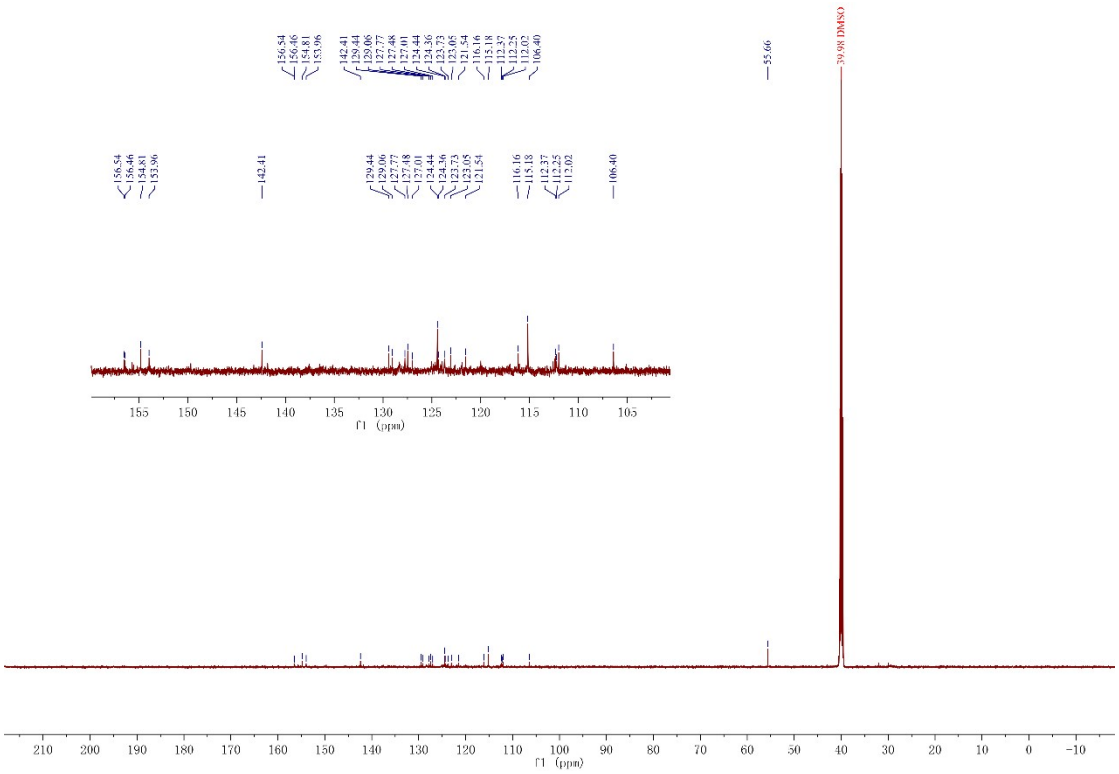

Figure S12. ^{13}C NMR spectrum of CX13 in DMSO.

Comment

Acquisition Paramet

Source Type	ESI	Ion Polarity	Positive	Set Nebulizer	0.4 Bar
Focus	Active	Set Capillary	4500 V	Set Dry Heater	180 °C
Scan Begin	50 m/z	Set End Plate	-500 V	Set Dry Gas	4.0 l/min
Scan End	1300 m/z	Set Charging	2000 V	Set Divert Valve	Source
		Set Corona	0 nA	Set APCI Heater	0 °C

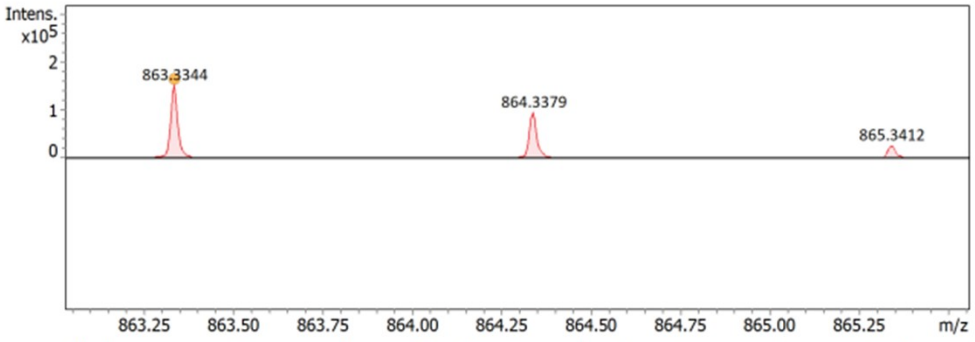

Meas. m/z	#	Ion Formula	m/z	err [ppm]	mSigma	# mSigma	Score	rdb	e¡¥ Conf	N-Rule
863.3344	1	C58H45N3O5	863.3359	1.7	25.9	1	100.00	38.0	even	ok

Figure S13. High resolution mass spectrometry of CX13.

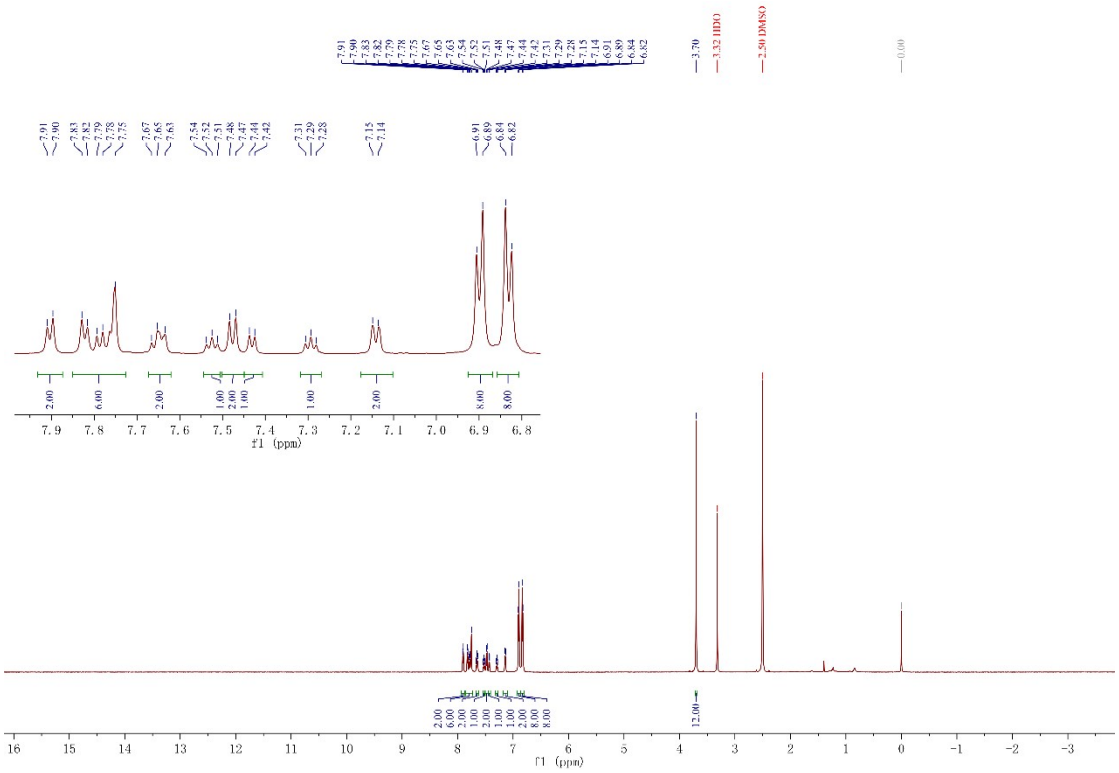

Figure S14. ^{1}H NMR spectrum of CX14 in DMSO.

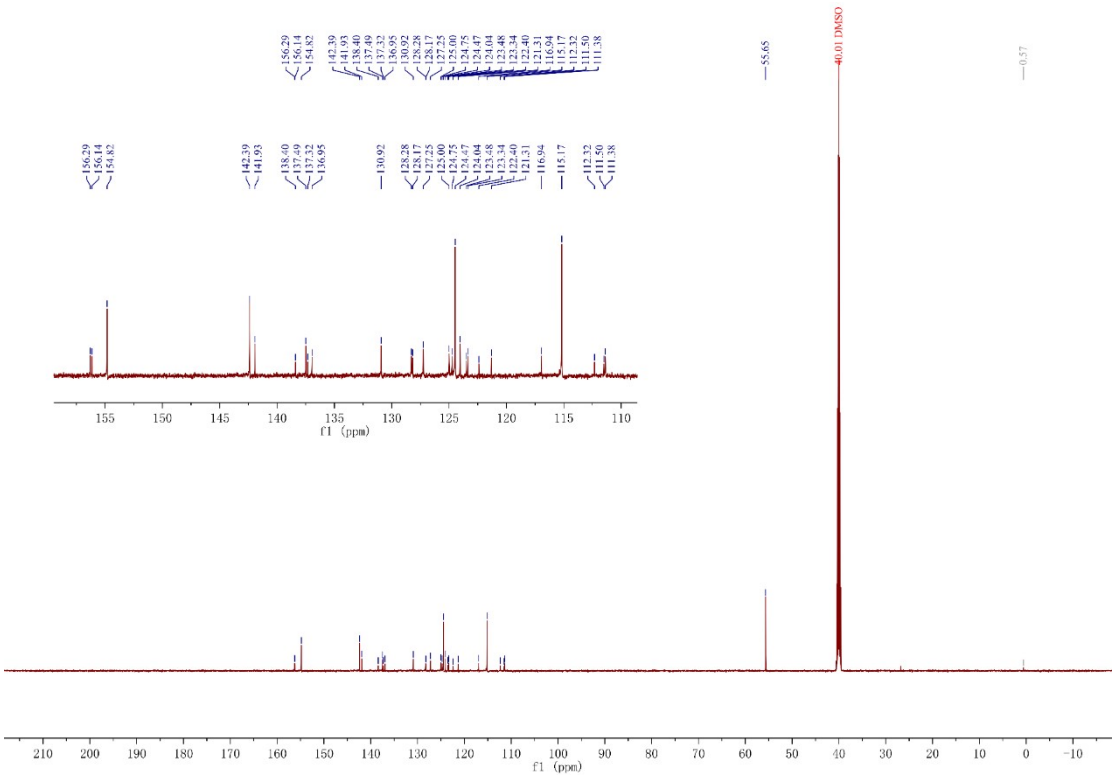

Figure S15. ^{13}C NMR spectrum of CX14 in DMSO.

Comment

Acquisition Paramet

Source Type	ESI	Ion Polarity	Positive	Set Nebulizer	0.4 Bar
Focus	Active	Set Capillary	4500 V	Set Dry Heater	180 °C
Scan Begin	50 m/z	Set End Plate	-500 V	Set Dry Gas	4.0 l/min
Scan End	1300 m/z	Set Charging	2000 V	Set Divert Valve	Source
		Set Corona	0 nA	Set APCI Heater	0 °C

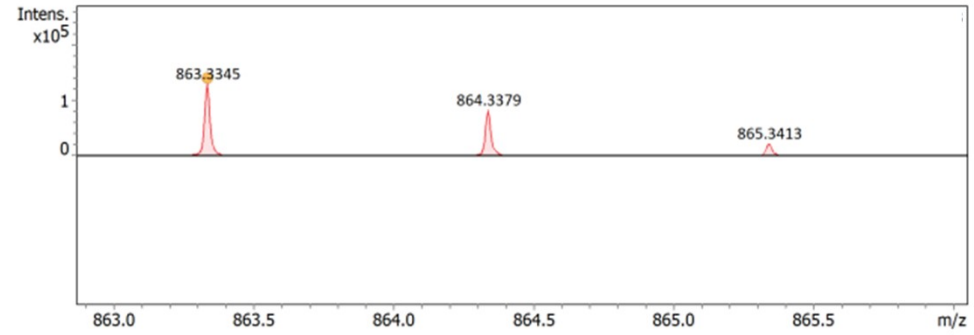

Meas. m/z	#	Ion Formula	m/z	err [ppm]	mSigma	# mSigma	Score	rdb	e¡¥ Conf	N-Rule
863.3345	1	C58H45N3O5	863.3359	1.7	26.9	1	100.00	38.0	even	ok

Figure S16. High resolution mass spectrometry of CX14.

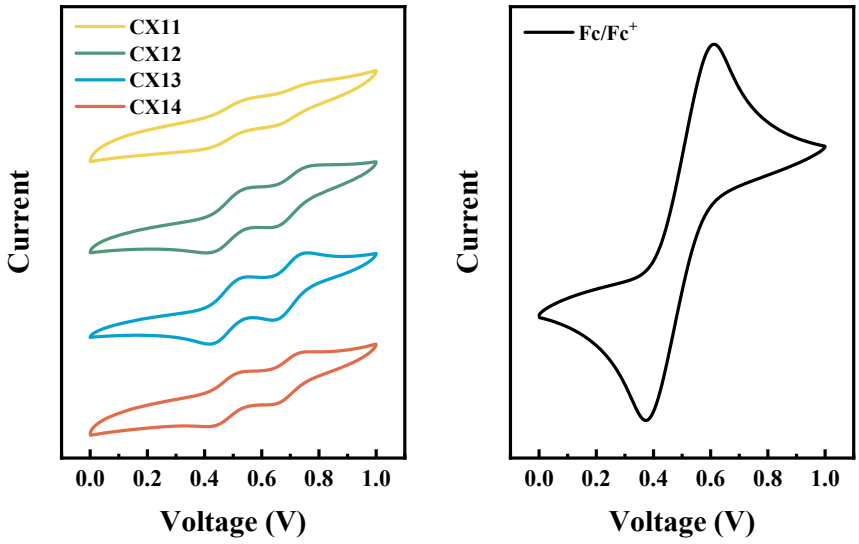

Figure S17. Cyclic voltammetry curve of CX11-CX14.

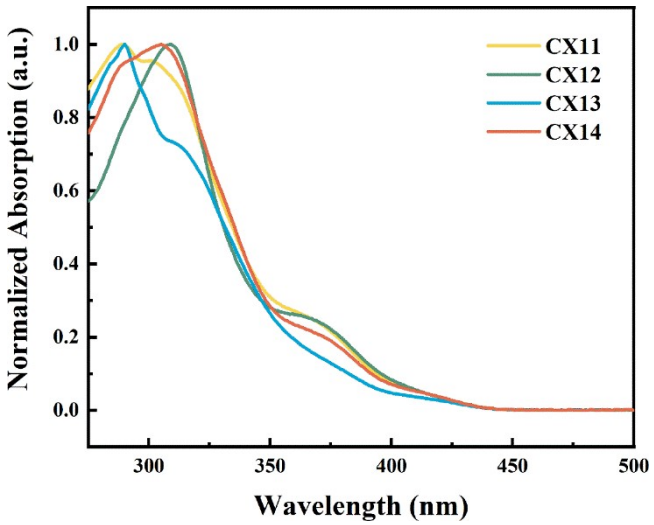

Figure S18 Absorption spectra of CX11-CX14 in DCM solution.

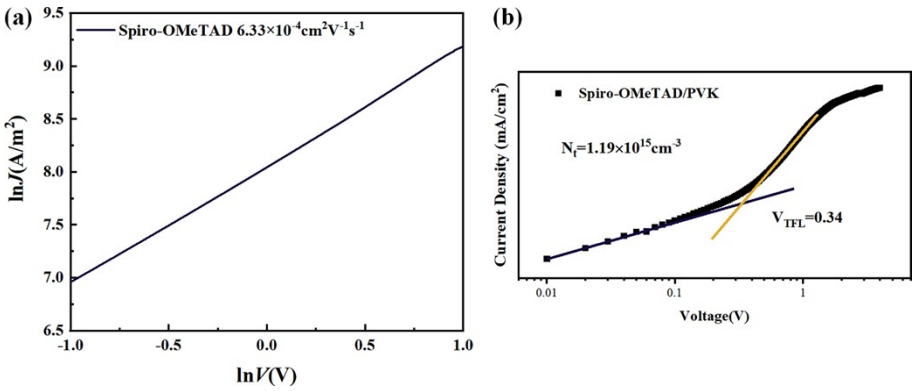

Figure S19 (a). J–V curve of Spiro-OMeTAD for the characterization of hole mobility. (b). J-V curve of Spiro-OMeTAD for the characterization of defect state.

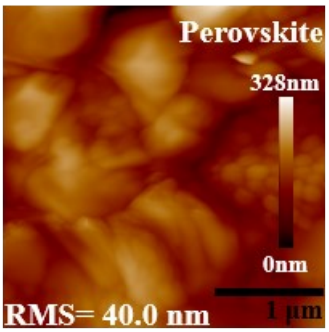

Figure S20 AFM image of perovskite film.

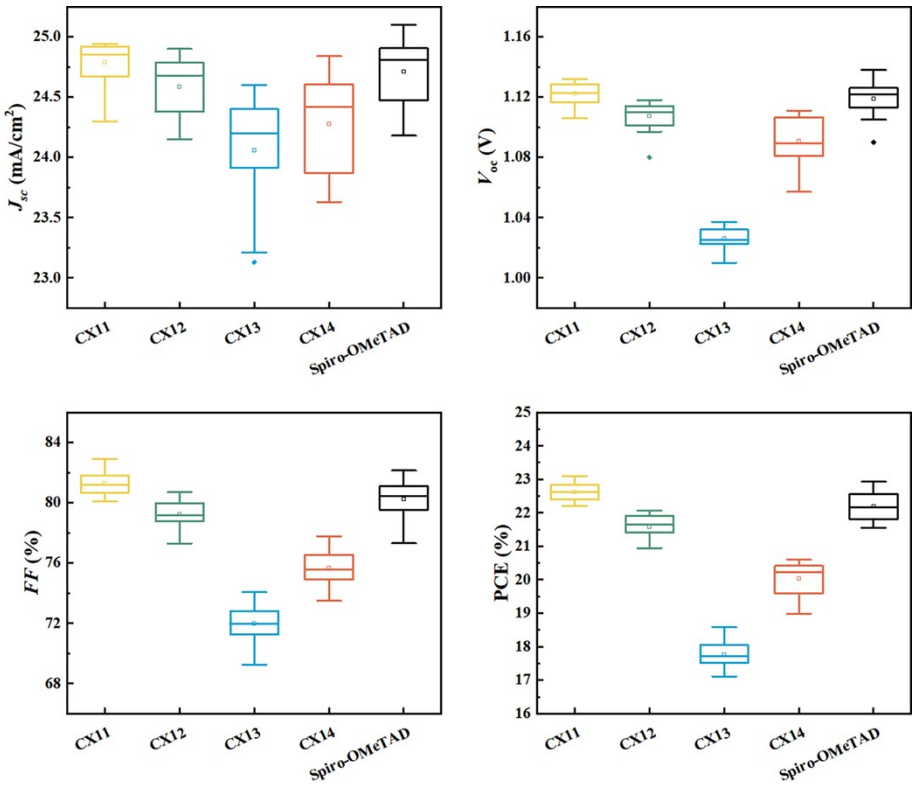

Figure S21 Box charts of the photovoltaic parameters of HTMs.

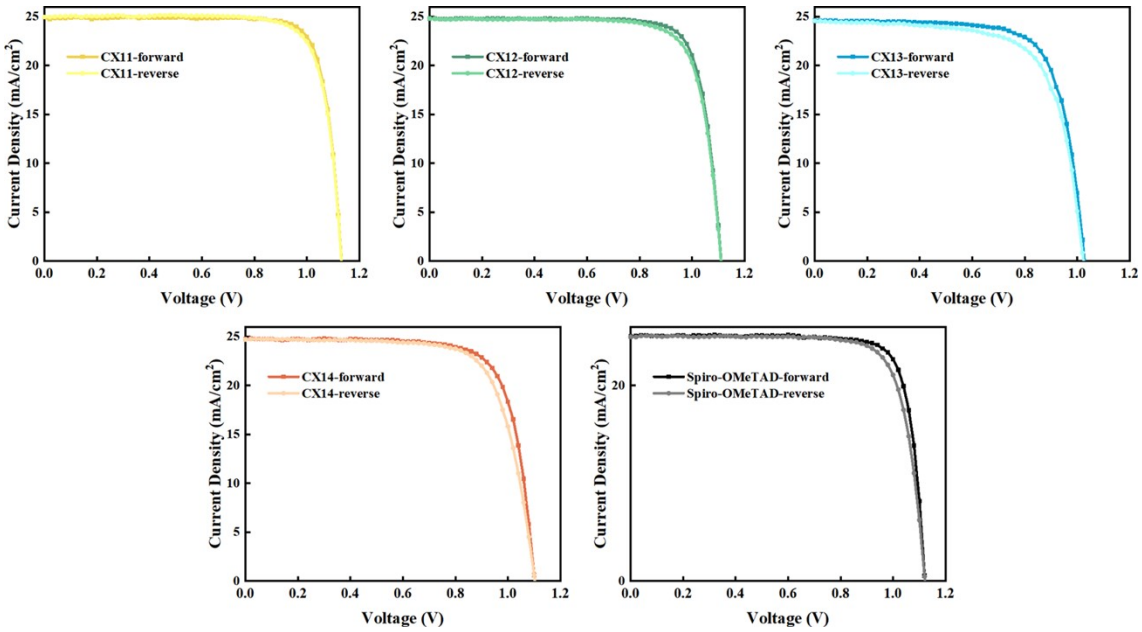

Figure S22 J−V curves under reverse and forward scan for HTMs based PSCs devices.

S3. Tables

Table S1 Interface adsorption energy of CX11-CX14.

	E_{PVK} [eV]	$E_{PVK/HTM}$ [eV]	E_{HTM} [eV]	E_{ads} [eV]
CX11	-3683.81	-2937.30	-742.62	-3.89
CX12	-3709.82	-2964.44	-741.85	-3.53
CX13	-3705.75	-2961.71	-741.96	-2.07
CX14	-3715.36	-2971.36	-740.55	-3.44

Table S2 EDA Analysis Result (in kcal/mol) for CX11-CX14 at B3LYP-D3(BJ)/6-31+G(d,p).

Dimer	ΔE_{int}	ΔE_{els}	ΔE_{xrep}	ΔE_{orb}	ΔE_{c}
CX11 Pathways 4	-24.89	-14.02 (19.56%)	46.78	-9.45(13.19%)	-48.19 (67.25%)
CX12 Pathways 5	-5.17	-5.22 (22.72%)	17.81	-3.49 (15.19%)	-14.27 (62.10%)
CX13 Pathways 1	-2.12	-0.60 (19.23%)	1.00	-0.49 (15.71%)	-2.03 (65.06%)
CX14 Pathways 6	-13.41	-5.68 (15.69%)	22.8	-4.90 (13.53%)	-25.63 (70.78%)

Table S3 Summary of hysteresis index (HI) and device performance of perovskite solar cell adopting CX11-CX14 at forward and reverse voltage scans.

HTMs		J_{sc}[mA/cm^2]	V_{oc}[V]	*FF*[%]	PCE[%]	HI (%) [a]
CX11	**forward**	24.93	1.132	81.82	23.09	2.08
	reverse	24.96	1.131	80.08	22.61	
CX12	**forward**	24.81	1.111	80.09	22.07	2.90
	reverse	24.81	1.1	77.84	21.43	
CX13	**forward**	24.6	1.028	73.51	18.58	5.97
	reverse	24.58	1.024	69.43	17.47	
CX14	**forward**	24.73	1.102	75.58	20.61	3.59
	reverse	24.71	1.103	72.91	19.87	
Spiro-OMeTAD	**forward**	25.01	1.121	81.78	22.93	4.01
	reverse	24.99	1.121	78.53	22.01	

[a] $HI=[(PCE_{forward} - PCE_{reverse})/PCE_{forward}]\times 100\%$

References

1 S. Ghosh, P. Verma, C. J. Cramer, L. Gagliardi and D. G. Truhlar, *Chem. Rev.*, 2018, **118**, 7249–7292.

2 X. Liu and X. Liu, *RSC Adv.*, 2019, **9**, 24733–24741.

3 J. Tomasi, B. Mennucci and R. Cammi, *Chem. Rev.*, 2005, **105**, 2999–3094.

4 M. J. Frisch, G. W. Trucks, H. B. Schlegel, G. E. Scuseria, M. A. Robb, J. R. Cheeseman, G. Scalmani, V. Barone, B. Mennucci, G. A. Petersson, H. Nakatsuji, M. Caricato, X. Li, H. P. Hratchian, A. F. Izmaylov, J. Bloino, G. Zheng, J. L. Sonnenberg, M. Hada, M. Ehara, K. Toyota, R. Fukuda, J. Hasegawa, M. Ishida, T. Nakajima, Y. Honda, O. Kitao, H. Nakai, T. Vreven, J. A. Montgomery Jr., J. E. Peralta, F. Ogliaro, M. Bearpark, J. J. Heyd, E. Brothers, K. N. Kudin, V. N. Staroverov, R. Kobayashi, J. Normand, K. Raghavachari, A. Rendell, J. C. Burant, S. S. Iyengar, J. Tomasi, M. Cossi, N. Rega, J. M. Millam, M. Klene, J. E. Knox, J. B. Cross, V. Bakken, C. Adamo, J. Jaramillo, R. Gomperts, R. E. Stratmann, O. Yazyev, A. J. Austin, R. Cammi, C. Pomelli, J. W. Ochterski, R. L. Martin, K. Morokuma, V. G. Zakrzewski, G. A. Voth, P. Salvador, J. J. Dannenberg, S. Dapprich, A. D. Daniels, Ö. Farkas, J. B. Foresman, J. V. Ortiz, J. Cioslowski and D. J. Fox, Gaussian∼09 revision A.01. Wallingford, CT: Gaussian, Inc., 2009.

5 J. M. Martínez and L. Martínez, *J. Comput. Chem.*, 2003, **24**, 819–825.

6 L. Martínez, R. Andrade, E. G. Birgin and J. M. Martínez, *J. Comput. Chem.*, 2009, **30**, 2157–2164.

7 D. Van Der Spoel, E. Lindahl, B. Hess, G. Groenhof, A. E. Mark and H. J. C. Berendsen, *J. Comput. Chem.*, 2005, **26**, 1701–1718.

8 G. Henkelman, A. Arnaldsson and H. Jónsson, *Comput. Mater. Sci.*, 2006, **36**, 354–360.

9 A. K. Rappe, C. J. Casewit, K. S. Colwell, W. A. I. Goddard and W. M. Skiff, *J. Am. Chem. Soc.*, 1992, **114**, 10024–10035.

10 J. Wang, R. M. Wolf, J. W. Caldwell, P. A. Kollman and D. A. Case, *J. Comput. Chem.*, 2004, **25**, 1157–1174.

11 C. I. Bayly, P. Cieplak, W. Cornell and P. A. Kollman, *J. Phys. Chem.*, 1993, **97**, 10269–10280.

12 T. Lu and F. Chen, *J. Comput. Chem.*, 2012, **33**, 580–592.

13 W. Humphrey, A. Dalke and K. Schulten, *J. Mol. Graph.*, 1996, **14**, 33–38.

14 C. Fonseca Guerra, J. G. Snijders, G. te Velde and E. J. Baerends, *Theor. Chem. Acc.*, 1998, **99**, 391–403.

15 V. Wang, N. Xu, J.-C. Liu, G. Tang and W.-T. Geng, *Comput. Phys. Commun.*, 2021, **267**, 108033.

16 J. Hafner and G. Kresse, in *Properties of Complex Inorganic Solids*, eds. A. Gonis, A. Meike and P. E. A. Turchi, Springer US, Boston, MA, 1997, pp. 69–82.

17 A. D. Becke and K. E. Edgecombe, *J. Chem. Phys.*, 1990, **92**, 5397–5403.

18 T. Lu and Q. Chen, *J. Phys. Chem. A*, 2023, **127**, 7023–7035.

19 T. Lu and Q. Chen, *Chemistry–Methods*, 2021, **1**, 231–239.

20 L. Zheng, X. Luo, X. Zhang, Y. Huang, L. Shen, F. Li, J. Yang, C. Tian, L. Xie and Z. Wei, *Adv. Funct. Mater.*, 2025, **35**, 2424464.